SCLF: Self-Contrastive Learning Framework for Hydrogen Leakage Traceability

Hui Zhang, Guangyao Fan, Jiaxin Zhang, Lizhi Zhang, Xuefang Li, and Bo Sun, *Member, IEEE*

***Abstract*— Hydrogen leakage traceability is crucial to ensuring hydrogen safety in the whole process of hydrogen production–storage–transport–application. However, due to the high cost of dismantling and testing, it is impractical to collect and label leakage locations for different leakage conditions. Traditional supervised learning methods lack generalization performance due to the difficulty of obtaining effective training on a limited number of labeled hydrogen leakage samples. Therefore, a self-contrastive learning framework (SCLF) is proposed in this study. Upstream of SCLF, a time–frequency fusion representation method based on self-contrastive learning (CL) is proposed to enhance domain-independent feature extraction, and a pretrained model (TF-FRM) is developed. Downstream of SCLF, a multirulebase fuzzy locator (MR-FL) based on fuzzy logic is proposed, which can locate the position of hydrogen leakage accurately by the representation based on TF-FRM. Finally, the proposed SCLF is tested on a real sensor signal, and its interpretability is also analyzed. Compared with other models, the SCLF demonstrates superior generalization, accuracy, and interpretability with limited supervised samples, achieving an average $F1$ score of 95.59%.**

***Index Terms*— Contrastive learning (CL), hydrogen safety, interpretability, representation learning.**

I. INTRODUCTION

HYDROGEN energy is green, low-carbon, and widely used with profound implications for addressing the depletion of fossil fuels and the global warming crisis [1]. As one of the most important carriers for the global energy transformation, hydrogen helps enable a transition to a net-zero carbon circular economy. However, hydrogen energy is facing increasing safety concerns, which are seriously hampering its further widespread applications [2].

Hydrogen normally exists at high pressure in the process of production–storage–transport–application and hydrogen leakage occurs from time to time. Due to the unique physical and chemical properties of hydrogen, combustion or even explosive accidents will occur when the leaking flammable hydrogen cloud encounters the ignition source, which directly threatens the safety of human life [3], [4], [5]. Quickly and accurately detecting and recognizing leakage faults before a hydrogen safety accident occurs, so that appropriate emergency planning measures can be taken. This will directly contribute to preventing further deterioration of the accident and reducing or even avoiding damage to life and property. Therefore, research on hydrogen leakage traceability is crucial to ensure the safety of the whole hydrogen energy industry chain and promote the sustainable development of hydrogen energy.

Hydrogen leakage traceability refers to the process of using certain technologies or methods to trace the source of a hydrogen leakage. In the field of hydrogen industry, especially in the case of hydrogen safety and environmental protection, hydrogen leakage traceability is important [6]. In recent years, the rapid development of artificial intelligence technology has made many researchers increasingly interested in developing new hydrogen leakage tracing methods.

Based on signals such as hydrogen concentration data collected by distributed sensors, machine learning (ML) [7] has been applied to the detection and identification of hydrogen leakage. Tian et al. [8] proposed a data-driven method based on a relevance vector machine for the leakage diagnosis of 70-MPa hydrogen storage tanks in hydrogen fuel-cell vehicles (HFCVs). Zhao et al. [9] studied the accuracy of K-nearest neighbor (KNN) and dynamic time-warping (K-DTW) algorithm for hydrogen leakage traceability in a confined space. Dhimish and Zhao [10] proposed a leakage detection and classification method based on an artificial neural network, and its effectiveness was verified on a 3-kW proton exchange membrane hydrogen fuel-cell system. However, ML usually requires more manual processing and expertise in feature engineering, which limits the accuracy of the above methods.

The deep learning (DL) [11], [12] with excellent adaptive feature extraction can reduce the reliance on manual feature extraction and physical modeling by experts [13]. As a result, DL-based methods have gradually become the mainstream paradigm for hydrogen leakage traceability. Deep belief neural network [14] were used in solid oxide fuel-cell systems. Taking renewable power-to-hydrogen system as the research target, Shi et al. [15] proposed a graph deep probability learning method to model the spatial–temporal dependence between the sequence data of different sensors, to obtain more comprehensive fault characteristics. Similarly, Li et al. [16] proposed a DL method based on gate recurrent unit

---

Received 17 December 2024; revised 14 March 2025; accepted 26 March 2025. Date of publication 15 April 2025; date of current version 28 April 2025. This work was supported by the National Key Research and Development Program of China under Grant 2023YFE0199100. The Associate Editor coordinating the review process was Dr. Gaigai Cai. *(Corresponding authors: Bo Sun; Xuefang Li.)*

Hui Zhang, Guangyao Fan, and Bo Sun are with the School of Control Science and Engineering, Shandong University, Jinan 250014, China (e-mail: 202234949@mail.sdu.edu.cn; 17866603773@163.com; sunbo@sdu.edu.cn).

Jiaxin Zhang and Xuefang Li are with the Institute of Thermal Science and Technology, Shandong University, Jinan 250014, China (e-mail: jiaxinz1998@163.com; lixf@email.sdu.edu.cn).

Lizhi Zhang is with the School of Reconnaissance, Shandong Police College, Jinan 250200, China (e-mail: zhanglizhi0518@163.com).

Digital Object Identifier 10.1109/TIM.2025.3560742

network acquiring spatial–temporal features automatically for the diagnosis task of fault in HFCVs. Recently, some feature processing techniques in the field of computer vision (CV) [17], [18], [19] have also been applied to the research of hydrogen leakage fault diagnosis. These studies typically combined multichannel sensor sequence data into images and then used convolutional neural networks (CNNs) to process the features. Bi et al. [20] proposed a hybrid DL model based on the CNN and long short-term memory (LSTM) network to accurately and efficiently detect and locate hydrogen leakage in hydrogen refueling stations (HRSs). As a CV classical model, ResNet was exploited by Yang et al. [21] to extract the distribution features from the hydrogen concentration sequences, combined with KNNs to identify the location and intensity of hydrogen leakage in HRSs. However, a large amount of data with labeled hydrogen leakage location is necessary for the above DL-based methods for model training and to accommodate deviations in data distribution under different hydrogen leakage conditions.

In practical hydrogen application scenarios, most hydrogen energy systems were required to be equipped with monitoring devices to ensure safety. These monitoring devices stored hydrogen concentration data by distributed sensors under normal conditions and leakage conditions. Unfortunately, workers were unable to find the exact location of the leakage when the leakage failure occurred, that is, manually labeling the leakage location of a large amount of hydrogen concentration data was expensive and not feasible. Therefore, there are the following unresolved problems for leakage traceability methods.

1) The characteristics of hydrogen sensor signals have not been fully studied, and the information features of multisource sensors have not been fully utilized, which will cause the generalization performance of leakage traceability methods to decline.
2) The DL is the mainstream paradigm in hydrogen leakage traceability and is often regarded as a opaque model without interpretability. The decisions of DL-based methods cannot be understood by humans, which will introduce a new risk point, and is detrimental to the safety of hydrogen.
3) Due to the high cost of dismantling and manual labeling, it is difficult to provide target-domain information containing all leakage locations for hydrogen leakage traceability methods. It is an urgent problem to reduce the dependence on supervised signals of hydrogen sensors.

To overcome these problems, a self-contrastive learning (CL) framework for hydrogen leakage traceability is proposed in this article. To our knowledge, this is the first report of CL in the field of hydrogen safety. Meanwhile, this study explores the interpretability of hydrogen leakage traceability first. Specifically, the main contributions and innovations of this article are as follows.

1) A time–frequency fusion representation method based on CL is proposed, which generates homogeneous and heterogeneous information of the hydrogen concentration sensor signal from the time and frequency domains to construct self-contrast pairs.

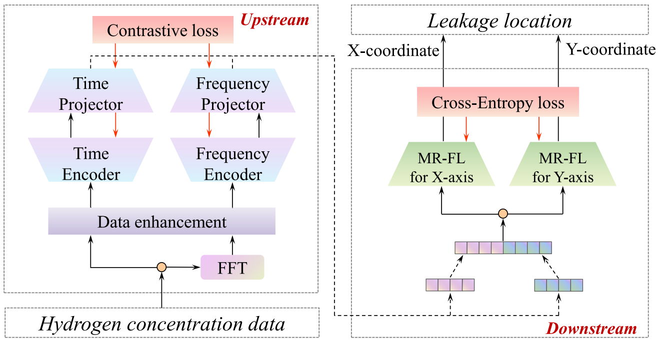

Fig. 1. Framework structure of the proposed SCLF. The black arrows indicate forward propagation, while the red arrows denote backpropagation.

2) A multirulebase fuzzy locator (MR-FL) based on fuzzy logic is proposed to deal with traceability tasks downstream according to representational information, and its interpretability advantages are discussed.
3) A self-CL framework (SCLF) is established, and a data-driven learning strategy of SCLF is developed to combine self-supervised learning and supervised learning.

The rest of the article is organized as follows. Section II describes the problem of hydrogen leakage traceability. Section III establishes the proposed SCLF. Experiments and analyses are described in Section IV. Section V concludes the article.

II. PROBLEM DESCRIPTION

In order not to lose commonality, J is used to represent the number of channels of the distributed sensors in hydrogen safety monitoring devices and L is used to represent the number of sampling points of each channel. Then, each sample of multisource hydrogen concentration sensor sequence data can be represented as a matrix

$$x = \begin{bmatrix} x_{1,1} & x_{1,2} & \cdots & x_{1,L} \\ x_{2,1} & x_{2,2} & \cdots & x_{2,L} \\ \vdots & \vdots & \ddots & \vdots \\ x_{J,1} & x_{J,2} & \cdots & x_{J,L} \end{bmatrix}. \tag{1}$$

The hydrogen leakage traceability aims to obtain a parameterized model $\mathcal{M}(\theta;\cdot)$ to map multisource hydrogen concentration sensor data to the specific leakage location

$$\left[y^x, y^y\right] = \mathcal{M}(\theta; x) \tag{2}$$

where $x \in \mathbb{R}^{J\times L}$, y^x, y^y is, respectively, the X coordinates and Y coordinates of the leakage location, θ is the parameter of $\mathcal{M}$, and $y^x \in \mathbb{N}_x$, $y^y \in \mathbb{N}_y$. The challenge of this problem is how to ensure the accuracy of leakage tracing in the absence of target domain information.

III. FRAMEWORK

An SCLF is proposed to solve the problem of hydrogen leakage traceability described in Section II, as shown in Fig. 1.

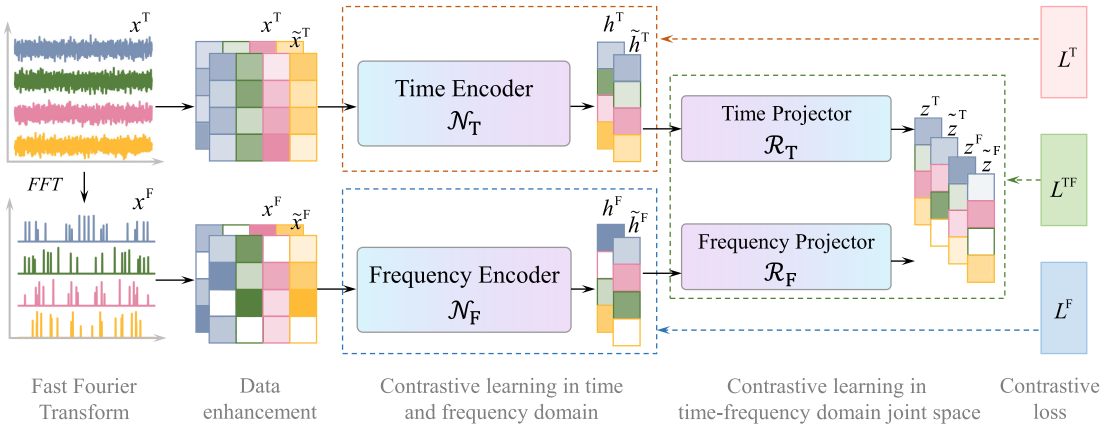

Fig. 2. Illustration of the proposed time–frequency fusion representation method. The pretrained model TF-FRM comprises a time encoder $\mathcal{N}_{\mathrm{T}}$, a frequency encoder $\mathcal{N}_{\mathrm{F}}$, a time projector $\mathcal{R}_{\mathrm{T}}$, and a frequency projector $\mathcal{R}_{\mathrm{F}}$.

A. Overview of the SCLF Framework

In the proposed SCLF, hydrogen leakage traceability is divided into upstream and downstream subtasks, as shown in Fig. 1.

Upstream, the representational time and frequency information of hydrogen concentration data is generated based on the proposed method in Section III-B by way of comparative learning, which is the key to maintaining good generalization. First, the representational domain of the hydrogen sensor signal is extended by fast Fourier transform (FFT) [22]. Second, data augmentation for raw concentration sequence and its discrete spectrum is used to reduce the dependence on hydrogen concentration data under different leakage conditions. Then, the time encoder and the frequency encoder learn the representations in independent time and frequency domains, respectively. Finally, the time projector and frequency projector map the independent time and frequency representations into a time–frequency domain joint space, to generate a fusion representation of time and frequency.

Downstream, two locators are developed based on the proposed MR-FL in Section III-C to locate the position of hydrogen leakage accurately. First, the fusion representations of time and frequency are connected as input features, which will be seen as the input feature of each locator, as shown in Fig. 1. Then, two MR-FLs learn the law between the input feature and the corresponding leakage location by supervised learning. Finally, the specific location of hydrogen leakage can be determined according to the X and Y coordinates predicted by the two MR-FLs.

B. Time–Frequency Fusion Representation Method

In recent years, some improved CL-based methods [23], [24] have been gradually applied to pattern recognition tasks in the industrial field [13], [25], such as domain-adaptive CL (DACL) [26] and conditional contrastive domain generalization (CCDG) [27]. CL-based methods have more significant generalization ability compared with DL- and ML-based methods [13]. Therefore, CL has the potential to solve the challenges of hydrogen leakage traceability.

However, the characteristics of the hydrogen sensor signals have not been fully studied. Only a single time domain can be used to produce comparison pairs, and the structural information of the raw hydrogen concentration data cannot be fully represented, which will directly lead to failed CL. Therefore, a time–frequency fusion representation method is proposed in this study.

Assume that N unlabeled multisource hydrogen concentration data samples are collected from the data acquisition system and expressed as $X_{\mathrm{pre}} = \{x_i | i = 1, 2, \ldots, N\}$.

1) Fast Fourier Transform: The frequency domain of the sensor signal is considered to obtain more structural information about the raw data and to achieve effective comparative learning. FFT is used to calculate the discrete spectrum of the raw data, as shown in Fig. 2. The raw sequence data is represented as $x_i^{\mathrm{T}} \equiv x_i$, and, correspondingly, the discrete spectrum is represented as x_i^{F}, that is,

$$x_i^{\mathrm{F}} = \mathrm{FFT}(x_i). \tag{3}$$

2) Data Enhancement: In the time domain, using jittering [28], scaling [29], time shifts, and neighborhood segments [30] exposes $\mathcal{N}_{\mathrm{T}}$ to more complex temporal dynamics. x_i^{T} with $\sim$ means time enhancement of the raw data, that is, $\tilde{x}_i^{\mathrm{T}}$. In the frequency domain, x_i^{F} can be enhanced by adding or deleting the frequency component to disturb the discrete spectrum of the raw hydrogen concentration sequence data. The frequency enhancement is represented as $\tilde{x}_i^{\mathrm{F}}$.

3) CL in the Time Domain: To learn the temporal representations of the raw data, the time encoder $\mathcal{N}_{\mathrm{T}}$ maps x_i^{T} and its enhancement $\tilde{x}_i^{\mathrm{T}}$ to the representations h_i^{T} and $\tilde{h}_i^{\mathrm{T}}$ in the time domain and can be expressed as

$$h_i^{\mathrm{T}} = \mathcal{N}_{\mathrm{T}}\left(\theta_{\mathrm{NT}}; x_i^{\mathrm{T}}\right); \quad \tilde{h}_i^{\mathrm{T}} = \mathcal{N}_{\mathrm{T}}\left(\theta_{\mathrm{NT}}; \tilde{x}_i^{\mathrm{T}}\right) \tag{4}$$

where $\mathcal{N}_{\mathrm{T}}(\theta_{\mathrm{NT}}; \cdot)$ is the mathematical model of the backbone network based on the Transformer [32] and θ_{NT} is the parameter of $\mathcal{N}_{\mathrm{T}}$. For another sample x_j^{T} and its enhancement $\tilde{x}_j^{\mathrm{T}}$, h_j^{T}, and $\tilde{h}_j^{\mathrm{T}}$ are generated by $\mathcal{N}_{\mathrm{T}}$. The positive pair of CL in the time domain is defined as $(h_i^{\mathrm{T}}, \tilde{h}_i^{\mathrm{T}})$, while the negative pairs are $(h_i^{\mathrm{T}}, h_j^{\mathrm{T}})$ and $(h_i^{\mathrm{T}}, \tilde{h}_j^{\mathrm{T}})$. The contrastive loss in the time domain is proposed to guide $\mathcal{N}_{\mathrm{T}}$ to learn the representations of time-enhanced invariance and can be expressed as

$$L_i^{\mathrm{T}} = \text{NT-Xent}\left(h_i^{\mathrm{T}}, \widetilde{h}_i^{\mathrm{T}}, X_{\mathrm{pre}}\right) = -\log \frac{\exp\left(\mathrm{sim}\left(h_i^{\mathrm{T}}, \widetilde{h}_i^{\mathrm{T}}\right)/\tau\right)}{\sum_{x_i^{\mathrm{T}} \in X_{\mathrm{pre}}} \delta_{i \neq j} \exp\left(\mathrm{sim}\left(h_i^{\mathrm{T}}, \mathcal{N}_{\mathrm{T}}\left(\theta_{\mathrm{NT}}; x_j^{\mathrm{T}}\right)\right)/\tau\right)} \quad (5)$$

where τ is a temporal parameter to adjust scale, $\delta_{i \neq j}$ is an indicator function, that equal 0 if $i \neq j$; otherwise, equal to 1; $\mathrm{sim}(u, v) = u^T v/||u||||v||$ denotes the cosine similarity.

4) CL in the Frequency Domain: The frequency encoder $\mathcal{N}_{\mathrm{F}}$ maps x_i^{F} and its enhancement $\widetilde{x}_i^{\mathrm{F}}$ to the representations h_i^{F} and $\widetilde{h}_i^{\mathrm{F}}$ in the frequency domain

$$h_i^{\mathrm{F}} = \mathcal{N}_{\mathrm{F}}\left(\theta_{\mathrm{NF}}; x_i^{\mathrm{F}}\right); \quad \widetilde{h}_i^{\mathrm{F}} = \mathcal{N}_{\mathrm{F}}\left(\theta_{\mathrm{NF}}; \widetilde{x}_i^{\mathrm{F}}\right). \quad (6)$$

The contrastive loss L_i^{F} is proposed to guide $\mathcal{N}_{\mathrm{F}}$ to learn the representations of frequency-enhanced invariance

$$L_i^{\mathrm{F}} = \text{NT-Xent}\left(h_i^{\mathrm{F}}, \widetilde{h}_i^{\mathrm{F}}, X_{\mathrm{pre}}\right) = -\log \frac{\exp\left(\mathrm{sim}\left(h_i^{\mathrm{F}}, \widetilde{h}_i^{\mathrm{F}}\right)/\tau\right)}{\sum_{x_i^{\mathrm{F}} \in X_{\mathrm{pre}}} \delta_{i \neq j} \exp\left(\mathrm{sim}\left(h_i^{\mathrm{F}}, \mathcal{N}_{\mathrm{F}}\left(\theta_{\mathrm{NF}}; x_j^{\mathrm{F}}\right)\right)/\tau\right)}. \quad (7)$$

5) Comparative Learning in Time–Frequency Domain Joint Space: Representations in the time and frequency domains are mapped to a joint space by the time projector $\mathcal{R}_{\mathrm{T}}$ and the frequency projector $\mathcal{R}_{\mathrm{F}}$, to ensure that the distance of representations between different domains is measurable

$$z_i^{\mathrm{T}} = \mathcal{R}_{\mathrm{T}}\left(\theta_{\mathrm{RT}}; h_i^{\mathrm{T}}\right); \quad \widetilde{z}_i^{\mathrm{T}} = \mathcal{R}_{\mathrm{T}}\left(\theta_{\mathrm{RT}}; \widetilde{h}_i^{\mathrm{T}}\right) \quad (8)$$

$$z_i^{\mathrm{F}} = \mathcal{R}_{\mathrm{F}}\left(\theta_{\mathrm{RF}}; h_i^{\mathrm{F}}\right); \quad \widetilde{z}_i^{\mathrm{F}} = \mathcal{R}_{\mathrm{F}}\left(\theta_{\mathrm{RF}}; \widetilde{h}_i^{\mathrm{F}}\right) \quad (9)$$

where z_i^{T} and z_i^{F} are the time representations and frequency representations of joint space, respectively, $\widetilde{z}_i^{\mathrm{T}}$ and $\widetilde{z}_i^{\mathrm{F}}$ are the corresponding enhancements, $\mathcal{R}_{\mathrm{T}}(\theta_{\mathrm{RT}}; \cdot)$ and $\mathcal{R}_{\mathrm{F}}(\theta_{\mathrm{RF}}; \cdot)$ are the mathematical model of the time projector and the frequency projector, respectively, and θ_{RT} and θ_{RF} are learnable parameters. The contrastive loss in the time–frequency domain joint space L_i^{TF} is proposed to realize the fusion of time and frequency representations, as follows:

$$L_i^{\mathrm{TF}} = L_i^{\mathrm{TF,T,\widetilde{F}}} + L_i^{\mathrm{TF,\widetilde{T},F}} + L_i^{\mathrm{TF,\widetilde{T},\widetilde{F}}} \quad (10)$$

where

$$L_i^{\mathrm{TF,T,\widetilde{F}}} = \text{NT-Xent}\left(z_i^{\mathrm{T}}, z_i^{\mathrm{F}}, X_{\mathrm{pre}}\right) - \text{NT-Xent}\left(z_i^{\mathrm{T}}, \widetilde{z}_i^{\mathrm{F}}, X_{\mathrm{pre}}\right) + \phi \quad (11)$$

$$L_i^{\mathrm{TF,\widetilde{T},F}} = \text{NT-Xent}\left(z_i^{\mathrm{T}}, z_i^{\mathrm{F}}, X_{\mathrm{pre}}\right) - \text{NT-Xent}\left(\widetilde{z}_i^{\mathrm{T}}, z_i^{\mathrm{F}}, X_{\mathrm{pre}}\right) + \phi \quad (12)$$

$$L_i^{\mathrm{TF,\widetilde{T},\widetilde{F}}} = \text{NT-Xent}\left(z_i^{\mathrm{T}}, z_i^{\mathrm{F}}, X_{\mathrm{pre}}\right) - \text{NT-Xent}\left(\widetilde{z}_i^{\mathrm{T}}, \widetilde{z}_i^{\mathrm{F}}, X_{\mathrm{pre}}\right) + \phi \quad (13)$$

where ϕ is a given constant margin. According to (10), the contrastive loss L_i^{TF} is used to minimize the distance between z_i^{T} and z_i^{F}, while pursuing the distance between larger enhanced representations, that is, z_i^{T} and $\widetilde{z}_i^{\mathrm{F}}$, $\widetilde{z}_i^{\mathrm{T}}$ and z_i^{F}, as well as $\widetilde{z}_i^{\mathrm{T}}$ and $\widetilde{z}_i^{\mathrm{F}}$.

Algorithm 1 Pretrain a TF-FRM Model

```
Require:
  $X_{\mathrm{pre}} = \{x_i | i = 1, 2, \ldots, N\}$: dataset; $N_{bs}$: size of batch;
  $K$: the maximum epochs; Adam optimizer.
Initialize:
  $\theta_{\mathrm{NT}}, \theta_{\mathrm{NF}}, \theta_{\mathrm{RT}}$ and $\theta_{\mathrm{RF}}$ are randomly initialized.
Compute:
  for $k = 1, \ldots, K$ do
      $N_{bs}$ samples were randomly selected from $X_{\mathrm{pre}}$;
      for $i = 1, \ldots, N_{bs}$ do
          $x_i^{\mathrm{T}} \leftarrow x_i, x_i^{\mathrm{F}} \leftarrow \mathrm{FFT}(x_i)$;
          Obtain $\widetilde{x}_i^{\mathrm{T}}$ and $\widetilde{x}_i^{\mathrm{F}}$ of $x_i^{\mathrm{T}}$ and $x_i^{\mathrm{F}}$;
          $h_i^{\mathrm{T}} \leftarrow \mathcal{N}_{\mathrm{T}}(\theta_{\mathrm{NT}}; x_i^{\mathrm{T}}); h_i^{\mathrm{F}} \leftarrow \mathcal{N}_{\mathrm{F}}(\theta_{\mathrm{NF}}; x_i^{\mathrm{F}})$;
          $\widetilde{h}_i^{\mathrm{T}} \leftarrow \mathcal{N}_{\mathrm{T}}(\theta_{\mathrm{NT}}; \widetilde{x}_i^{\mathrm{T}}); \widetilde{h}_i^{\mathrm{F}} \leftarrow \mathcal{N}_{\mathrm{F}}(\theta_{\mathrm{NF}}; \widetilde{x}_i^{\mathrm{F}})$;
          Calculate $L_i^{\mathrm{T}}, L_i^{\mathrm{F}}$;
          $z_i^{\mathrm{T}} \leftarrow \mathcal{R}_{\mathrm{T}}(\theta_{\mathrm{RT}}; h_i^{\mathrm{T}}); z_i^{\mathrm{F}} \leftarrow \mathcal{R}_{\mathrm{F}}(\theta_{\mathrm{RF}}; h_i^{\mathrm{F}})$;
          $\widetilde{z}_i^{\mathrm{T}} \leftarrow \mathcal{R}_{\mathrm{T}}(\theta_{\mathrm{RT}}; \widetilde{h}_i^{\mathrm{T}}); \widetilde{z}_i^{\mathrm{F}} \leftarrow \mathcal{R}_{\mathrm{F}}(\theta_{\mathrm{RF}}; \widetilde{h}_i^{\mathrm{F}})$;
          Calculate $L_i^{\mathrm{TF,T,\widetilde{F}}}$, $L_i^{\mathrm{TF,\widetilde{T},F}}$ and $L_i^{\mathrm{TF,\widetilde{T},\widetilde{F}}}$;
          $L_i^{\mathrm{TF}} \leftarrow L_i^{\mathrm{TF,T,\widetilde{F}}} + L_i^{\mathrm{TF,\widetilde{T},F}} + L_i^{\mathrm{TF,\widetilde{T}v,\widetilde{F}}}$;
          $L^R \leftarrow \lambda(L_i^{\mathrm{T}} + L_i^{\mathrm{F}}) + (1 - \lambda)L_i^{\mathrm{TF}}$;
          Update $\theta_{\mathrm{NT}}, \theta_{\mathrm{NF}}, \theta_{\mathrm{RT}}, \theta_{\mathrm{RF}}$ via Adam [31].
      end
  end
```

Finally, the proposed time–frequency fusion representation method guides the TF-FRM model to pretrain on unlabeled hydrogen concentration data (i.e., X_{pre}) and minimize the total loss L^R

$$L^R = \lambda\left(L_i^{\mathrm{T}} + L_i^{\mathrm{F}}\right) + (1 - \lambda)L_i^{\mathrm{TF}} \quad (14)$$

where λ is used to control the relative importance. Detailed steps are given in Algorithm 1.

C. Multirulebase Fuzzy Locator

Assume that the dataset composed of the multisource hydrogen concentration data with the leakage location label can be expressed as $X_{\mathrm{fine}} = \{x_i', y_i'\}_{i=1}^{N'}$, where N' is the number of samples. For the ith sample, TF-FRM calculates the time and frequency representations, that is, $z_i'^{\mathrm{T}}$ and $z_i'^{\mathrm{F}}$, respectively, which are treated as inputs to the proposed MR-FL and expressed as $z_i' = [z_i'^{\mathrm{T}}, z_i'^{\mathrm{F}}]$, where $z_i' \in \mathbb{R}^D$ and D is the dimension of z_i'.

Assuming that there are C hydrogen leakage locations, the proposed MR-FL will adaptively generate C rulebases, as shown in Fig. 3. The cth hydrogen leakage location is identified by the cth rulebase. Each rule has the construction form of IF-THEN [33], [34], take the rth rule in the cth rulebase as an example

$$\text{IF}: z_{i,1}' \text{ is } \widetilde{X}_{r,1}, \quad \text{and}, \ldots, \text{and } z_{i,D}' \text{ is } \widetilde{X}_{r,D}$$

$$\text{THEN}: y_r^c\left(z_i'\right) = b_r^c + \sum_{d=1}^{D} \omega_{r,d}^c \times z_{i,d}' \quad (15)$$

where b_r^c and $\omega_{r,d}^c$ are bias and weight parameters of the rth rule, respectively, and $\widetilde{X}_{r,1}$ is a fuzzy set [35] used to calculate

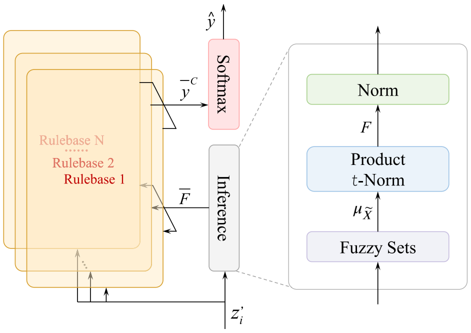

Fig. 3. Schematic of the proposed MR-FL.

Algorithm 2 Mathematical Model of MR-FL

```
Require:
  $z_i' \in \mathbb{R}^D$.
Compute:
  for $r = 1, 2, \ldots, R$ do
      for $d = 1, 2, \ldots, D$ do
          $\mu_{\widetilde{X}_{r,d}}(z_{i,d}') \leftarrow \exp\left[-\frac{(z_{i,d}' - c_{r,d})^2}{2\sigma_{r,d}^2}\right]$,
      end
  end
  for $r = 1, 2, \ldots, R$ do
      $F_r(z_i') \leftarrow \prod_{d=1}^{D} \mu_{\widetilde{X}_{r,d}}(z_{i,d}')$;
  end
  for $c = 1, 2, \ldots, C$ do
      $\overline{F}_r(z_i') \leftarrow \frac{F_r(z_i')}{\sum_{k=1}^{R} F_k(z_i')}$;
      for $r = 1, 2, \ldots, R$ do
          $y_r^c \leftarrow \sum_{d=1}^{D} \omega_{r,d}^c \times z_{i,d}' + b_r^c$;
      end
      $\overline{y}_R^c \leftarrow \sum_{r=1}^{R} \overline{F}_r \times y_r^c$;
  end
  $\overline{y}^C \leftarrow [\overline{y}_R^1, \ldots, \overline{y}_R^C]$;
  $y^C \leftarrow \frac{\exp(\overline{y}_R^c)}{\sum_{c=1}^{C} \exp(\overline{y}_R^c)}$;
  $\widehat{y} \leftarrow \text{argmax}(y^C)$.
```

the membership degree μ of $z_{i,1}'$. For all rules in the cth rulebase, the bias parameters form a vector $b^c \in \mathbb{R}^R$ and the weight parameters form a matrix $\omega^c \in \mathbb{R}^{R \times D}$. The output of R rules can be computed as

$$y_R^c = \omega^c z_i' + b^c \tag{16}$$

where $y_R^c \in \mathbb{R}^R$. Each rule of each rulebase is fired by firing degree $\overline{F}_r$ of inference

$$\overline{y}_R^c = \sum_{r=1}^{R} \overline{F}_r \times y_r^c \tag{17}$$

where $\overline{y}_R^c \in \mathbb{R}$, $\overline{y}_r^c \in \mathbb{R}^R$, and $\overline{F}_r^c \in \mathbb{R}^R$. The aggregate output of all rulebases is expressed as $\overline{y}^C = [\overline{y}_R^1, \ldots, \overline{y}_R^C] \in \mathbb{R}^C$. Then, $\overline{y}^C$ is convert to y^C by Softmax as follows:

$$y^C = \frac{\exp(\overline{y}_R^c)}{\sum_{c=1}^{C} \exp(\overline{y}_R^c)} \tag{18}$$

where $y^C \in \mathbb{R}^C$. Finally, the predicted hydrogen leakage location $\widehat{y} \in \mathbb{N}$ of MR-FL is obtained by argmax [36]

$$\widehat{y} = \text{argmax}(y^C). \tag{19}$$

The detailed mathematical model of MR-FL is given in Algorithm 2.

D. Data-Driven Learning Strategy of the SCLF

The SCLF is required to complete self-supervised learning and supervised learning tasks in the upstream and downstream, respectively. Therefore, the data-driven learning strategy of the SCLF is developed, which adopts the pretraining + fine-tuning mechanism and divides the learning task into three stages, as shown in Fig. 4.

In the first stage, the TF-FRM model consisting of $\mathcal{N}_\text{T}$, $\mathcal{N}_\text{F}$, $\mathcal{R}_\text{T}$, and $\mathcal{R}_\text{F}$ is pretrained on the multisource hydrogen concentration data without labeled leakage location (i.e., $X_\text{pre} = \{x_i | i = 1, 2, \ldots, N\}$). Despite the lack of supervisory signals to guide TF-FRM model training, CL loss (i.e., L^R), encourages the TF-FRM model to fuse representational information of multiple domains and enrich the feature scales, which is beneficial to improving generalization performance.

In the second stage, the TF-FRM model and two MR-FLs are fine-tuned on the multisource hydrogen concentration data with labeled leakage location (i.e., $X_\text{fine} = \{x_i', y_i'^x, y_i'^y\}_{i=1}^{N'}$). First, the time and frequency representations (i.e., z_i') are generated by the pretrained TF-FRM on X_fine. Second, z_i' is seen as the input feature of two MR-FLs. Third, specific leakage locations can be predicted by two MR-FLs. Then, the cross-entropy loss [37] is used to minimize the difference between the real leakage location and the predicted leakage location. Considering that learning the data distribution of the fine-tuning dataset is beneficial to TF-FRM, the model parameters of the pretrained TF-FRM are also further optimized and adjusted. Finally, according to the CL losses and cross-entropy loss, all parameters of the TF-FRM model and two MR-FLs are optimized and adjusted by the Adam [31] optimizer in the same backpropagation.

In the third stage, a well-trained TF-FRM model and two MR-FLs are evaluated on the testing dataset, and the performance is measured by statistical indicators.

IV. EXPERIMENT

The hydrogen leakage experiment was conducted in a specific hydrogen energy application scenario, that is, an underground garage and 827 sets of real concentration sensor signals were collected. Then, comparison and ablation experiments were performed to verify the performance of the proposed SCLF.

A. Setup

A 1:24 scale underground garage model was designed and constructed to reproduce the hydrogen leakage and diffusion behavior of HFCVs in confined space in practical applications, as shown in Fig. 5. The size of the underground garage model was 24 × 150 × 250 cm^3, and there was an opening with a

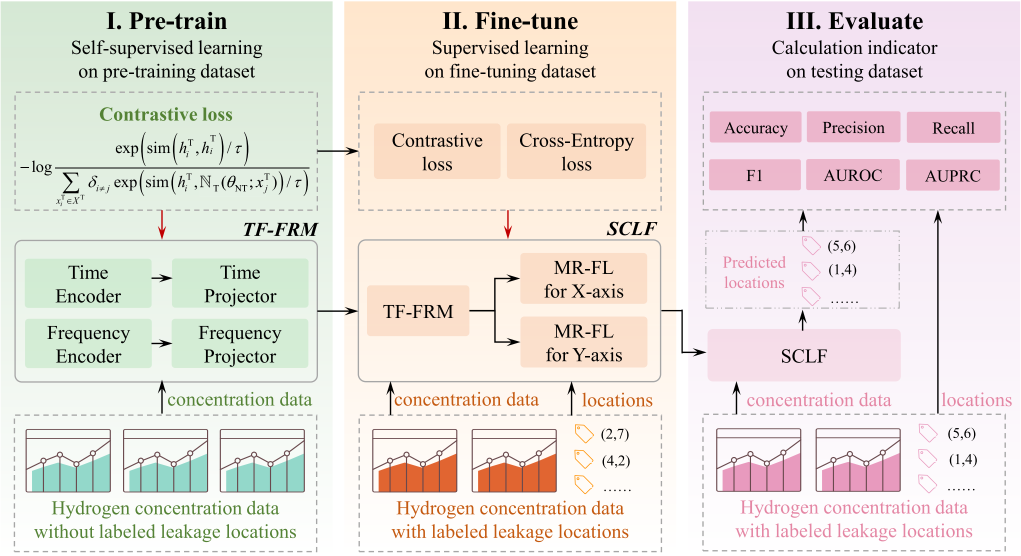

Fig. 4. Illustration of the data-driven learning strategy. In the first stage, the TF-FRM is pretrained using multisource hydrogen concentration data without labeled leakage locations. In the second stage, both the TF-FRM and the two MR-FLs are fine-tuned on multisource hydrogen concentration data with labeled leakage locations. In the third stage, the well-trained SCLF is evaluated on the testing dataset. In this figure, the black arrows indicate forward propagation, while the red arrows denote backpropagation.

length of 24.4 cm and a height of 13.3 cm to maintain the pressure balance in the space during the experiment. There were a total of 80 parking spaces where HFCVs with potential hydrogen leakage parked.

The experiment was conducted in an indoor environment with a temperature of 24 °C and a humidity of 55%. Helium, which is physically close to hydrogen, was used as an alternative gas for hydrogen in consideration of experimental safety. A typical family car model (MINI COOPER, 1/24) was used as the leaking HFCVs in the experiment. As shown in Fig. 5, the leak point was placed at the bottom of the vehicle model to simulate the most common and dangerous leakage conditions. A standard 40-L helium cylinder with a flow rate of 3.4 SLPM was used to create a momentum-dominated leak jet from a 35-MPa hydrogen storage tank. The experimental system used reducing valves, pressure transducer, and other instruments to ensure the stability of the flow during the experiment.

Twelve concentration sensors (XEN-TGC3880Pt) were equipped to measure the helium concentration of the HFCV model after leakage. All sensor was installed on the ceiling of the garage model to minimize the impact on airflow. The data acquisition system of Agilent (34970A) was used to communicate with the distributed sensor and obtain the sensor signal in real time, with a frequency of 1.4 Hz. Before the start of each experiment, the sensors were calibrated according to the method described in [9], and the voltage signals of sensors were converted into the concentration signals of helium. The collected distributed helium concentration data was stored in a computer.

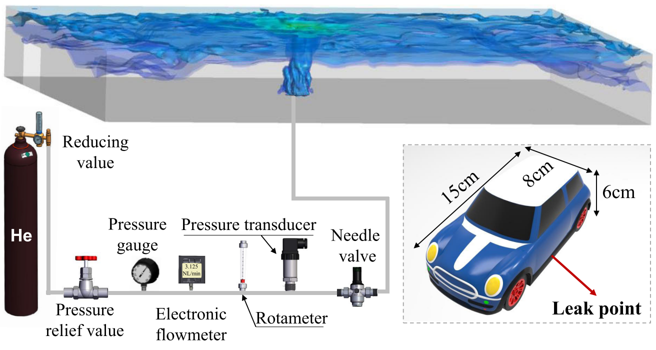

Fig. 5. Schematic of the experimental system.

B. Comparison Methods and Evaluation Indicators

1) Comparison Methods: To fully evaluate the performance of the proposed framework, the SCLF is compared with ML-based methods, DL-based methods, and CV-based methods. Specifically, ML-based methods include multilayer perceptron (MLP) [9], K-DWT [9], support vector machines (SVMs) [38], and extreme learning machine (ELM) [39]. ML-based methods extract features manually according to the method in [9]. DL-based methods include LSTM [20] and Transformers [32], which require no additional feature processing and treat the complete hydrogen concentration sequence data as the input of the model. Classical CV-based methods include CNNs [20] and ResNet [21], which treated hydrogen concentration sequence data collected from 12 distributed sensors as single-channel images as input. In addition, 227 sets of real sensor signals are labeled with the leakage locations, manually. The remaining sensor signals are used for pretraining of the proposed SCLF.

The hyperparameter settings for the SCFL are provided as follows. In the TF-FRM, the network architectures of the time encoder and frequency encoder are adopted from [32], while the network architectures of the time projector and the frequency projector are illustrated in Fig. 6. The batch size for both the pretraining and fine-tuning processes is determined based on the recommendations in [33]. Since the number of rulebases (i.e., C) in MR-FL adaptively varies with the number

TABLE I

PERFORMANCE INDICATORS (X-COORDINATE)

		K-DWT	ANN	SVM	ELM	LSTM	Transformer	CNN	ResNet	SCLF
Accuracy	train	0.8672±0.0321	0.9441±0.0437	0.8647±0.0103	0.8478±0.0191	1.0000±0.0000	1.0000±0.0000	1.0000±0.0000	1.0000±0.0000	0.9805±0.0011
	test	0.6832±0.0145	0.7264±0.0119	0.6367±0.0148	0.7290±0.0214	0.7732±0.0095	0.8632±0.0391	0.8642±0.0247	0.8619±0.0784	**0.9090±0.0117**
Precision	train	0.8358±0.0213	0.7031±0.0197	0.7053±0.0104	0.7282±0.0093	1.0000±0.0000	1.0000±0.0000	1.0000±0.0000	1.0000±0.0000	0.9229±0.0201
	test	0.6313±0.0152	0.7912±0.0394	0.8038±0.0123	0.7040±0.0561	0.7893±0.0338	0.7731±0.0428	0.8126±0.0142	0.8191±0.0457	**0.9540±0.0119**
Recall	train	0.7975±0.0493	0.7818±0.0579	0.7737±0.0105	0.7587±0.0094	1.0000±0.0000	1.0000±0.0000	1.0000±0.0000	1.0000±0.0000	0.9282±0.0304
	test	0.7758±0.0143	0.7696±0.0452	0.8129±0.0125	0.7246±0.0109	0.8605±0.0589	0.8473±0.0583	0.8962±0.0302	0.8415±0.0141	**0.9543±0.0203**
F1 score	train	0.7980±0.0414	0.7337±0.0458	0.7286±0.0102	0.7349±0.0100	1.0000±0.0000	1.0000±0.0000	1.0000±0.0000	1.0000±0.0000	0.9249±0.0211
	test	0.7064±0.0144	0.7153±0.0146	0.8783±0.0125	0.7071±0.0106	0.7546±0.0162	0.7929±0.0604	0.8435±0.0203	0.8282±0.0585	**0.9540±0.0149**
AUROC	train	0.8763±0.0319	0.8547±0.0382	0.8856±0.0114	0.8760±0.0108	0.9991±0.0098	1.0000±0.0000	1.0000±0.0000	1.0000±0.0000	0.9991±0.0213
	test	0.8096±0.0376	0.7965±0.0242	0.8794±0.0123	0.8558±0.0107	0.9375±0.0131	0.9371±0.0092	0.9715±0.0146	0.9171±0.0154	**0.9892±0.0406**
AUPRC	train	0.8865±0.0513	0.8460±0.0334	0.8607±0.0109	0.8181±0.0098	0.9984±0.0109	1.0000±0.0000	1.0000±0.0000	1.0000±0.0000	0.9945±0.0204
	test	0.7983±0.0237	0.7475±0.0163	0.8463±0.0121	0.7232±0.0105	0.8475±0.0224	0.9147±0.0163	0.8387±0.0127	0.8272±0.0222	**0.9643±0.0174**

of leakage locations, the number of rulebases for the MR-FL used to locate the X-coordinate is set to 20, while that for the other MR-FL is set to 4. Sensitivity analysis is conducted for several critical hyperparameters, including the number of time–frequency features (i.e., D), the weight coefficient of the contrastive loss (i.e., λ), and the learning rate of the Adam optimizer [31], as detailed in Section IV-F.

All comparison experiments were conducted on a desktop computer with an i5-12600KF Intel processor, 32 GB RAM, and RTX 4060 Ti GPU. All comparison methods were implemented in Python.

2) Evaluation Indicators: To accurately measure the performance of the proposed SCLF and comparison methods, six different indicators are used in the experiments to comprehensively measure the recognition performance, which includes accuracy, precision, recall, $F1$ score, AUROC, and AUPRC.

C. Comparative Experimental Results and Analysis

The performance of ML-based methods, DL-based methods, CV-based methods, and the proposed SCLF on hydrogen leakage traceability task is evaluated. To enhance the rigor and reliability of the experimental results and further validate the superior performance of the proposed SCLF, we conducted sixfold cross-validation and provided corresponding statistical results in the comparative experiments.

First of all, Tables I and II, respectively, provide six statistical indicators of X and Y-coordinates predicted by different methods. The proposed SCLF achieves the best performance in the hydrogen leakage traceability task, with an average $F1$ score of 95.59%. DL- and CV-based methods often have better performance than ML-based methods. For example, the accuracy of LSTM, Transformers, CNNs, and ResNet can even reach 100% during the training phase. This is because DL- and CV-based methods have better adaptive feature extraction capabilities than ML-based methods, which is critical for accurately identifying leaking information. Although the proposed SCLF fails to obtain sufficiently compelling training indicators, its test performance is the most significant, especially in comparison with DL- and CV-based methods. For example, the $F1$ score of the proposed SCLF decreases by 4.41% compared to ResNet during the training phase, but improves by 8.82% during the testing phase, as shown in Tables I and II. This means that the proposed SCLF has more significant generalization performance, that is, it can still predict the leakage locations accurately on unanticipated hydrogen concentration data.

D. SCLF with Spatial Features

Hydrogen concentration signals are collected through distributed sensors, where the relative positions and relationships between sensors often contain critical information that may facilitate hydrogen leakage traceability. To further analyze multisource hydrogen concentration data, an SCLF with spatial features (SCLF-SF) is proposed. Specifically, the multisource data collected by distributed hydrogen concentration sensors are modeled as a graph structure, where each sensor is represented as a node, and the node features correspond to the concentration signals of the sensors. The edge weights between nodes are determined by the Euclidean distance between the sensors. This graph structure effectively captures the spatial relationships within the sensor network, providing essential topological information for subsequent hydrogen leakage traceability tasks. To incorporate the spatial features of multisource hydrogen concentration data, necessary modifications were made to the previous SCLF. Specifically, graph convolutional networks (GCNs) are employed to replace the Transformer as the backbone network for the time encoder and the frequency encoder in Fig. 2. This is because GCNs are generally regarded as a promising approach for capturing spatial dependencies between sensor signals [40], [41]. The details of these modifications are illustrated in Fig. 6.

The experimental results demonstrate that the proposed SCLF framework maintains robust performance even after replacing its backbone encoder, highlighting the architectural resilience of SCLF. However, although SCLF-SF shows potential in capturing spatial features, its performance improvement in hydrogen leakage traceability tasks is not statistically significant. Specifically, on the test set, SCLF-SF achieves the

TABLE II

PERFORMANCE INDICATORS (Y-COORDINATE)

		K-DWT	ANN	SVM	ELM	LSTM	Transformer	CNN	ResNet	SCLF
Accuracy	train	0.7897±0.0362	0.7495±0.0523	0.9816±0.0046	0.8470±0.0301	1.0000±0.0000	1.0000±0.0000	1.0000±0.0000	1.0000±0.0000	0.9819±0.0056
	test	0.6833±0.0481	0.7280±0.0427	0.7276±0.0481	0.6824±0.0504	0.7734±0.0463	0.8640±0.0387	0.8185±0.0340	0.8641±0.0306	**0.9548±0.0049**
Precision	train	0.8127±0.0383	0.7807±0.0470	0.9769±0.0032	0.7555±0.0357	1.0000±0.0000	1.0000±0.0000	1.0000±0.0000	1.0000±0.0000	0.9694±0.0063
	test	0.5198±0.0461	0.7450±0.0530	0.6989±0.0475	0.4831±0.0518	0.8008±0.0390	0.8379±0.0446	0.7515±0.0397	0.8753±0.0229	**0.9520±0.0044**
Recall	train	0.6938±0.0440	0.8112±0.0332	0.9825±0.0023	0.7029±0.0297	1.0000±0.0000	1.0000±0.0000	1.0000±0.0000	1.0000±0.0000	0.9858±0.0030
	test	0.6515±0.0451	0.8705±0.0294	0.8426±0.0406	0.5618±0.0513	0.7507±0.0399	0.8436±0.0377	0.8221±0.0351	0.8994±0.0287	**0.9683±0.0035**
F1 score	train	0.6986±0.0373	0.7270±0.0347	0.9762±0.0046	0.7085±0.0311	1.0000±0.0000	1.0000±0.0000	1.0000±0.0000	1.0000±0.0000	0.9765±0.0061
	test	0.5663±0.0471	0.6186±0.0432	0.7995±0.0396	0.5074±0.0459	0.7466±0.0382	0.8180±0.0314	0.7627±0.0369	0.9149±0.0204	**0.9577±0.0057**
AUROC	train	0.9625±0.0034	0.9391±0.0173	0.9781±0.0023	0.9970±0.0012	0.9995±0.0004	1.0000±0.0000	1.0000±0.0000	1.0000±0.0000	0.9999±0.0003
	test	0.9298±0.0185	0.8969±0.0214	0.9491±0.0107	0.9260±0.0202	0.9378±0.0116	0.9629±0.0078	0.9723±0.0054	**0.9889±0.0043**	0.9839±0.0026
AUPRC	train	0.8919±0.0065	0.8811±0.0082	0.8980±0.0043	0.9685±0.0026	0.9985±0.0006	1.0000±0.0000	1.0000±0.0000	1.0000±0.0000	0.9994±0.0002
	test	0.8707±0.0183	0.8474±0.0124	0.8463±0.0148	0.9475±0.0053	0.9474±0.0038	0.8872±0.0220	0.8582±0.0205	0.9413±0.0082	**0.9524±0.0041**

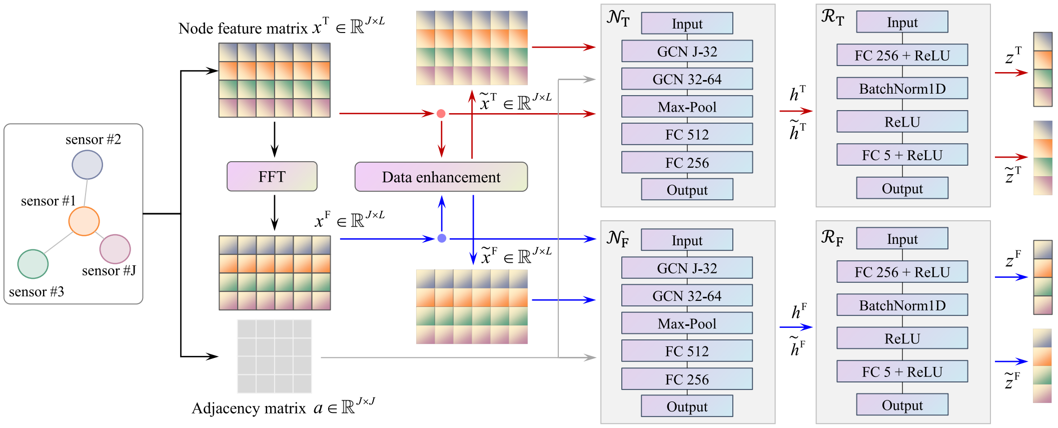

Fig. 6. Diagram of the TF-FRM in the SCLF-SF framework. In this figure, the symbol definitions are consistent with those in Fig. 2. The matrix $x \in \mathbb{R}^{J\times L}$, as described in Section II, is constructed from the multisource hydrogen concentration sensor sequence data and serves as the nodal feature matrix in this diagram. The adjacency matrix of the graph is constructed based on the Euclidean distance between sensors. The red arrow denotes the computation process associated with representations in the time domain, the blue arrow indicates the computation process related to representations in the frequency domain, and the gray arrow represents the spatial feature information of the distributed hydrogen concentration sensors. The complete structure of SCLF-SF is provided in Fig. 1.

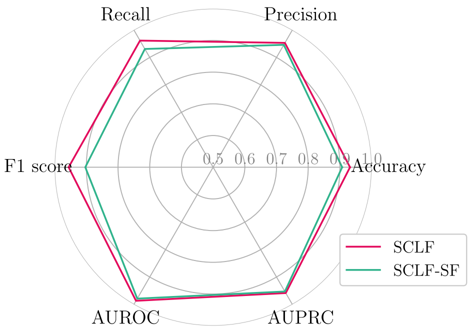

Fig. 7. Performance comparison between the SCLF and the SCLF-SF.

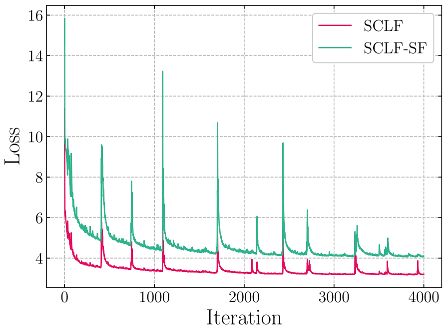

Fig. 8. Pretraining loss of the SCLF and the SCLF-SF.

following evaluation indicators: an accuracy of 0.9071, a precision of 0.9459, a recall of 0.9308, an $F1$ score of 0.9033, an AUROC of 0.9787, and an AUPRC of 0.9528. In comparison to the previous SCLF framework, these indicators exhibit reductions of 2.66%, 0.75%, 3.17%, 5.50%, 0.80%, and 0.58%, respectively, as depicted in Fig. 7. Despite utilizing the same CL loss function L_R and conducting training over the same 4000 iterations, the loss value of the pretrained TF-FRM model in SCLF-SF remains notably higher than that of SCLF, as shown in Fig. 8. This means that the integration of spatial features into the TF-FRM may impede the ability of SCLF to effectively capture the time–frequency consistency inherent

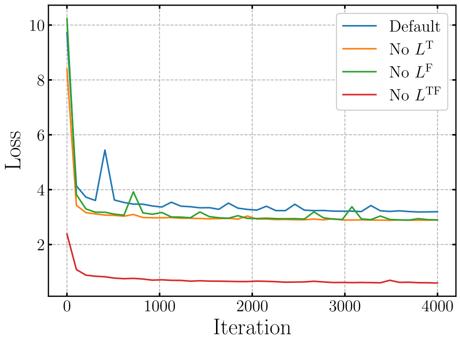

Fig. 9. Pretraining loss of the TF-FRM in the first ablation experiment.

TABLE III
TESTING INDICATORS OF DIFFERENT SCLFS IN THE FIRST ABLATION EXPERIMENT

		Default	No L^{T}	No L^{F}	No L^{TF}
Accuracy	train	**0.9812±0.0034**	0.8932±0.0351	0.9025±0.0181	0.9529±0.0411
	test	**0.9319±0.0083**	0.7905±0.0236	0.8726±0.0241	0.9018±0.0540

in hydrogen concentration signals. Consequently, we conclude that the direct incorporation of spatial features into the current SCLF framework may not represent the optimal strategy.

E. Ablation Experiments

The performance improvements of these key components in SCLF were validated through ablation experiments. To ensure the reliability of the experimental results, all ablation experiments were repeated five times, and the average accuracy metrics were reported. In the first ablation experiment, the default pretrained model was the complete TF-FRM, followed by the individual removal of different components to evaluate the interactions between various contrastive losses, as illustrated in Fig. 9. Specifically, when the contrastive loss in the time domain is removed, the time encoder ceases to contribute to the TF-FRM. Similarly, without the contrastive loss in the frequency domain as a self-supervised signal, the frequency encoder also becomes ineffective. Furthermore, in the absence of the CL in the time–frequency domain joint space, the time encoder and the frequency encoder can still operate independently. The SCLF based on the default TF-FRM achieves the best performance, as shown in Table III. This means that the default TF-FRM can generate generalizable representations for downstream hydrogen leakage location prediction, and the ability of the ablated models to represent time–frequency features gradually diminishes as CL components are successively removed. The independent contribution of the time encoder is significantly higher than that of the frequency encoder, as evidenced by the 9.41% improvement in the accuracy indicator for SCLF without L_F compared to SCLF without L_T. Additionally, CL in the time–frequency domain joint space contributes to more significant performance gains for SCLF. Without the contrastive term L_R, the accuracy indicator of SCLF decreases by 3.23%.

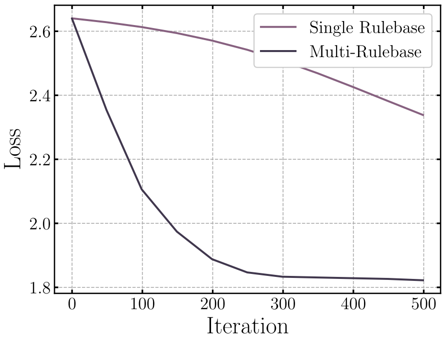

Fig. 10. Testing losses of different MR-FLs in the second ablation experiment.

TABLE IV
INDICATORS OF DIFFERENT MR-FLS DOWNSTREAM IN THE SECOND ABLATION EXPERIMENT

Indicators	Single Rulebase (traditional)	Multi-Rulebase (ours)	Improvement
Accuracy	0.7272±0.0267	**0.9319±0.0083**	21.96%↑
Precision	0.6161±0.0383	**0.9530±0.0082**	35.35%↑
Recall	0.7397±0.0168	**0.9613±0.0119**	23.05%↑
F1 score	0.6809±0.0230	**0.9559±0.0103**	28.76%↑
AUROC	0.9781±0.0143	**0.9866±0.0216**	0.86%↑
AUPRC	0.8576±0.0196	**0.9584±0.0108**	10.52%↑

TABLE V
EFFECT OF THE NUMBER OF TIME AND FREQUENCY FEATURES ON THE SCLF

D	4	6	8	10	12	14
Train loss	2.3384	2.0536	1.8701	1.8221	1.7815	**1.7842**
Test loss	2.3936	2.1440	1.9941	1.9588	1.8429	**1.8187**
Test Recall	0.9504	0.9561	0.9587	0.9613	0.9662	**0.9695**

In the second ablation experiment, the contribution of multirulebase to overall performance is investigated. MR-FL with multirulebase can achieve rapid convergence during training, while fuzzy locators with single rulebase are far behind, as shown in Fig. 10. In addition, the accuracy, precision, recall, $F1$ score, AUROC, and AUPRC of the MR-FL with multirulebase are improved by 21.96%, 35.35%, 23.05%, 28.76%, 0.86% and 10.52%, respectively, compared with that without multirulebase, as shown in Table IV. Therefore, the multirulebase is necessary for the proposed MR-FL.

F. Parameter Sensitivity

To validate the computational stability of the proposed SCLF framework, the sensitivity analysis was conducted on several key hyperparameters. Each experiment was repeated five times, and the average results were reported. An increase in the number of time–frequency features implies that the upstream TF-FRM can capture more local and global temporal and frequency information from the hydrogen concentration data, thereby better characterizing the dynamic properties of the signals. This also serves as a favorable factor for the

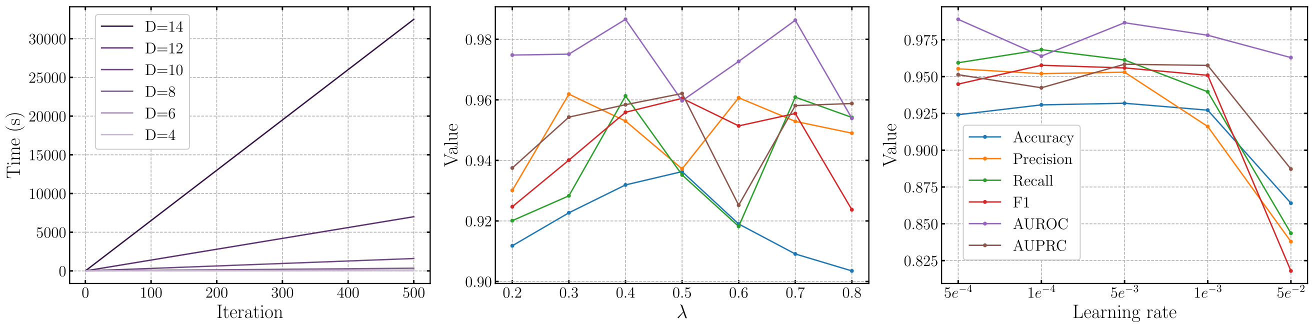

(a) (b) (c)

Fig. 11. Effects of different hyperparameters on SCLF performance: (a) number of time–frequency features; (b) weight coefficient for different losses; and (c) learning rate.

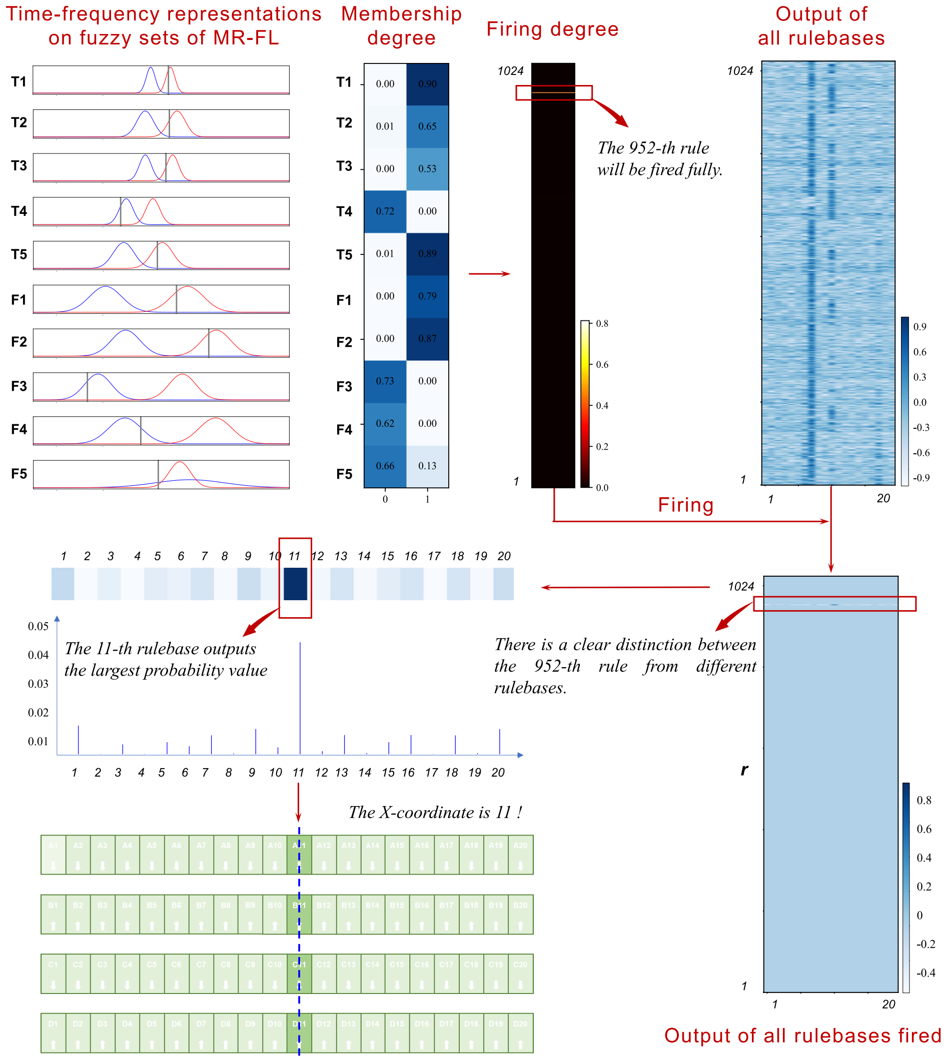

Fig. 12. Schematic of interpretability of the SCLF, which is analyzed and discussed with the X-coordinate of the leakage location as an example.

significant improvement in the test accuracy of the downstream MR-FLs, as shown in Table V. Meanwhile, the number of time–frequency features significantly affects the computational time of the downstream MR-FLs, as shown in Fig. 11(a). This is because these features are concatenated as the input to each MR-FL, and the increase in input dimensionality directly leads to a sharp rise in the number of rules in the rulebase of each MR-FL. To balance the performance and computational cost of SCLF, the number of time–frequency features was set to 10 for pretraining, fine-tuning, and testing in the remaining experiments of this study. As shown in Fig. 11(b), SCLF achieves optimal performance across multiple metrics when $\lambda = 0.4$. An excessively high λ may cause TF-FRM to overly focus on independent tasks in either the time or frequency domain, neglecting the consistent representation of time–frequency characteristics. Similarly, an excessively low λ is also unsuitable for self-CL in TF-FRM. According to Fig. 11(c), a learning rate that is too high can easily lead to overfitting, while a learning rate that is too low may be insufficient to extract adequate generalized features from the limited hydrogen concentration data. A learning rate of 5×10^{-3} achieves the best performance and was selected as the training benchmark for the remaining experiments in this study. The proposed SCLF exhibits varying performance levels due to differences in these hyperparameter values. Nevertheless, SCLF maintains stable test accuracy across a wide range of parameter settings, as demonstrated in Table V and Fig. 11. This means that the proposed SCLF exhibits a certain degree of robustness in the selection of these hyperparameters.

G. Interpretability of the SCLF

The interpretability of the proposed SCLF framework is analyzed in detail with a randomly selected sample of multisource hydrogen concentration sensor data. The following content is analyzed and discussed with the X-coordinate of the leakage location as an example. Fine-tuned TF-FRM generate five time representations and five frequency representations, respectively, as shown in Fig. 12. Each representation is described by two fuzzy sets of MR-FL for the X-axis, and the shape of each fuzzy set is determined by the mean and standard deviation of the Gaussian membership function (i.e., μ). The membership degree of all time and frequency representations is plotted in the form of a heat map, and the firing degree is further calculated. In the heat map of firing degree, the 952nd value is the largest, which means that the 952nd rule will be fired to the greatest extent. The heat map in the upper right corner of Fig. 12 shows the rule output values under different rulebases, and each rulebase has 1024 rules. In the heat map in the lower right corner of Fig. 12, the output of multiple rulebases fired is shown according to (17). The contribution of rules other than the 952nd rule to the final output is almost negligible by comparing the two heat maps, which means that the 952nd rule is the dominant rule for MR-FL to make decisions of traceability. More surprisingly, the 952nd rule can be written in concrete form under the current sample, taking the first rulebase as an example

$$\begin{aligned}\text{IF}:\ & T1 \text{ is } X_{1,2}, T2 \text{ is } X_{2,2}, T3 \text{ is } X_{3,2}, T4 \text{ is } X_{4,1}\\ & T5 \text{ is } X_{5,2}, F1 \text{ is } X_{6,2}, F2 \text{ is } X_{7,2}, F2 \text{ is } X_{8,1}\\ & F4 \text{ is } X_{9,1}, F5 \text{ is } X_{10,1}\\ \text{THEN}:\ & y_{952}^{1} = 0.4192\end{aligned} \tag{20}$$

where y_{952}^{1} is calculated according to (16). Therefore, we can clearly understand the inference mechanism of the proposed MR-FL by IF-THEN form rules in (15).

Although the 952nd rule is most actively fired, there are significant differences among the different rulebases, as shown in the heat map at the bottom right corner of Fig. 12, which is helpful to analyze the output of the entire rulebases. It can be clearly found that the output of the 11th rulebase is the largest, and the probability is also the largest after processing by SoftMax. Therefore, the X-coordinate for the leakage position inferenced by the MR-FL is 11.

Based on the above analysis, it can be concluded that the proposed SCLF has undoubtedly significant interpretability, which is different from other opaque models, although it also has to follow a complex computational process.

V. CONCLUSION

It is expensive and impractical to manually label the hydrogen leakage location and obtain a large number of supervised learning samples, which presents technical challenges to traditional hydrogen leakage tracing methods. Therefore, this study proposes an SCLF. The results demonstrated that the proposed SCLF can effectively solve the downstream hydrogen leakage traceability task. Compared with other methods based on ML, DL, and CV, the proposed SCLF can show more remarkable precision and generalization on previously unexpected hydrogen concentration data and achieves an average testing $F1$ score of 95.59%. In addition, the interpretability of the proposed SCLF is analyzed, and its rule-based inference mechanism can be understood by humans easily, which is beneficial to hydrogen safety.

Finally, it is important to note that the spatial features of distributed hydrogen concentration sensor data may contain critical patterns of anomaly propagation, which could potentially benefit the self-supervised learning capabilities of the proposed SCLF framework. In addition, the dataset in this study is relatively limited, and different scenarios and larger data datasets should be used to evaluate the performance of SCLF. These aspects represent key directions for our future research.

REFERENCES

[1] J. Xu, Q. Li, J. Li, Z.-H. Zhang, and L. Zheng, "Robust design of a green hydrogen supply chain under spatiotemporal imbalance," *IEEE Trans. Autom. Sci. Eng.*, early access, Apr. 2, 2024, doi: 10.1109/TASE.2024.3381449.

[2] M. Ö. Balta and M. T. Balta, "Development of a sustainable hydrogen city concept and initial hydrogen city projects," *Energy Policy*, vol. 166, Jul. 2022, Art. no. 113015.

[3] X. He et al., "Prediction model for the evolution of hydrogen concentration under leakage in hydrogen refueling station using deep neural networks," *Int. J. Hydrogen Energy*, vol. 51, pp. 702–712, Jan. 2024.

[4] Y. Shao, Y. Yin, S. Du, and L. Xi, "A surface connectivity-based approach for leakage channel prediction in static sealing interface," *J. Tribol.*, vol. 141, no. 6, Jun. 2019, Art. no. 062201.

[5] Y. Shao, Y. Yin, S. Du, T. Xia, and L. Xi, "Leakage monitoring in static sealing interface based on three dimensional surface topography indicator," *J. Manuf. Sci. Eng.*, vol. 140, no. 10, Oct. 2018, Art. no. 101003.

[6] J. A. Gordon, N. Balta-Ozkan, and S. A. Nabavi, "Socio-technical barriers to domestic hydrogen futures: Repurposing pipelines, policies, and public perceptions," *Appl. Energy*, vol. 336, Apr. 2023, Art. no. 120850.

[7] S. A. A. Qadri, N.-F. Huang, T. M. Wani, and S. A. Bhat, "Advances and challenges in computer vision for image-based plant disease detection: A comprehensive survey of machine and deep learning approaches," *IEEE Trans. Autom. Sci. Eng.*, vol. 22, pp. 2639–2670, 2025.

[8] Y. Tian, Q. Zou, Z. Jin, and Z. Lin, "Data-driven diagnosis of the high-pressure hydrogen leakage in fuel cell vehicles based on relevance vector machine," *Int. J. Hydrogen Energy*, vol. 47, no. 24, pp. 12281–12292, Mar. 2022.

[9] M. Zhao et al., "Leak localization using distributed sensors and machine learning for hydrogen releases from a fuel cell vehicle in a parking garage," *Int. J. Hydrogen Energy*, vol. 46, no. 1, pp. 1420–1433, Jan. 2021.

[10] M. Dhimish and X. Zhao, "Enhancing reliability and lifespan of PEM fuel cells through neural network-based fault detection and classification," *Int. J. Hydrogen Energy*, vol. 48, no. 41, pp. 15612–15625, May 2023.

[11] J. Wang et al., "A hybrid deep learning-based framework for chip packaging fault diagnostics (Don't short) in X-ray images," *IEEE Trans. Ind. Informat.*, vol. 20, no. 9, pp. 11181–11191, Sep. 2024.

[12] G. He, Y. Ding, Z. Wu, X. Chen, D. Zhang, and J. Song, "Environment-adaptive online learning for portable energy storage based on porous electrode model," *IEEE Trans. Autom. Sci. Eng.*, vol. 22, pp. 8386–8399, 2025.

[13] Y. He, C. Zhao, and W. Shen, "Cross-domain compound fault diagnosis of machine-level motors via time–frequency self-contrastive learning," *IEEE Trans. Ind. Informat.*, vol. 20, no. 7, pp. 9692–9701, Jul. 2024.

[14] X. Zhang, J. Zhou, and W. Chen, "Data-driven fault diagnosis for PEMFC systems of hybrid tram based on deep learning," *Int. J. Hydrogen Energy*, vol. 45, no. 24, pp. 13483–13495, May 2020.

[15] J. Shi, X. Zhang, H. Zhang, Q. Wang, J. Yan, and L. Xiao, "Automated detection and diagnosis of leak fault considering volatility by graph deep probability learning," *Appl. Energy*, vol. 361, May 2024, Art. no. 122939.

[16] D. Li, Z. Zhang, L. Zhou, P. Liu, Z. Wang, and J. Deng, "Multi-time-step and multi-parameter prediction for real-world proton exchange membrane fuel cell vehicles (PEMFCVs) toward fault prognosis and energy consumption prediction," *Appl. Energy*, vol. 325, Nov. 2022, Art. no. 119703.

[17] X. Zhou et al., "Computer vision enabled building digital twin using building information model," *IEEE Trans. Ind. Informat.*, vol. 19, no. 3, pp. 2684–2692, Mar. 2023.

[18] M. Wang, T. Su, S. Chen, W. Yang, J. Liu, and Z. Wang, "Automatic model-based dataset generation for high-level vision tasks of autonomous driving in haze weather," *IEEE Trans. Ind. Informat.*, vol. 19, no. 8, pp. 9071–9081, Aug. 2023.

[19] W. Ren et al., "Facial expression monitoring via fine-grained vision-language alignment," *IEEE Trans. Autom. Sci. Eng.*, vol. 22, pp. 7492–7505, 2025.

[20] Y. Bi et al., "Hydrogen leakage location prediction at hydrogen refueling stations based on deep learning," *Energy*, vol. 284, Dec. 2023, Art. no. 129361.

[21] G. Yang, D. Kong, X. He, X. Yu, and K. Jiang, "Prediction of hydrogen leakage location and intensity in hydrogen refueling stations based on deep learning," *Int. J. Hydrogen Energy*, vol. 68, pp. 209–220, May 2024.

[22] J. Zhao, Y. Zhou, J. Zhao, J. Song, and F. Dong, "Precision position measurement of PMSLM based on ApFFT and temporal sinusoidal fringe pattern phase retrieval," *IEEE Trans. Ind. Informat.*, vol. 16, no. 12, pp. 7591–7601, Dec. 2020.

[23] X. Wu, C.-D. Wang, J.-Q. Lin, W.-D. Xi, and P. S. Yu, "Motif-based contrastive learning for community detection," *IEEE Trans. Neural Netw. Learn. Syst.*, vol. 35, no. 9, pp. 11706–11719, Sep. 2024.

[24] B. Ye, J. Lai, and X. Xie, "Teacher-student collaboration: Effective semi-supervised model for defect instance segmentation," *IEEE Trans. Autom. Sci. Eng.*, vol. 22, pp. 6932–6943, 2025.

[25] P. Peng, J. Lu, T. Xie, S. Tao, H. Wang, and H. Zhang, "Open-set fault diagnosis via supervised contrastive learning with negative out-of-distribution data augmentation," *IEEE Trans. Ind. Informat.*, vol. 19, no. 3, pp. 2463–2473, Mar. 2023.

[26] Y. An, K. Zhang, Y. Chai, Q. Liu, and X. Huang, "Domain adaptation network base on contrastive learning for bearings fault diagnosis under variable working conditions," *Expert Syst. Appl.*, vol. 212, Feb. 2023, Art. no. 118802.

[27] M. Ragab et al., "Conditional contrastive domain generalization for fault diagnosis," *IEEE Trans. Instrum. Meas.*, vol. 71, pp. 1–12, 2022.

[28] C. Ian Tang, I. Perez-Pozuelo, D. Spathis, and C. Mascolo, "Exploring contrastive learning in human activity recognition for healthcare," 2020, *arXiv:2011.11542*.

[29] E. Eldele et al., "Time-series representation learning via temporal and contextual contrasting," 2021, *arXiv:2106.14112*.

[30] D. Kiyasseh, T. Zhu, and D. A. Clifton, "CLOCS: Contrastive learning of cardiac signals across space, time, and patients," in *Proc. Int. Conf. Mach. Learn. (ICML)*, Jul. 2021, pp. 5606–5615.

[31] Q. Xu et al., "Primary multiplicative noise suppression in the HTEM system via adaptive momentum estimation and elastic-net regularized framework," *IEEE Trans. Instrum. Meas.*, vol. 73, pp. 1–10, 2024.

[32] A. Vaswani et al., "Attention is all you need," in *Proc. Conf. NIPS*, Dec. 2017, pp. 6000–6010.

[33] D. Wu, Y. Yuan, J. Huang, and Y. Tan, "Optimize TSK fuzzy systems for regression problems: Minibatch gradient descent with regularization, DropRule, and AdaBound (MBGD-RDA)," *IEEE Trans. Fuzzy Syst.*, vol. 28, no. 5, pp. 1003–1015, May 2020.

[34] Y. Cui, D. Wu, and J. Huang, "Optimize TSK fuzzy systems for classification problems: Minibatch gradient descent with uniform regularization and batch normalization," *IEEE Trans. Fuzzy Syst.*, vol. 28, no. 12, pp. 3065–3075, Dec. 2020.

[35] C. Treesatayapun, "Quantum inference fuzzy rules network model free adaptive control for discontinuous derivative discrete-time systems," *IEEE Trans. Autom. Sci. Eng.*, vol. 22, pp. 5051–5060, 2025.

[36] Y. Deng, L. Wang, H. Jia, X. Tong, and F. Li, "A sequence-to-sequence deep learning architecture based on bidirectional GRU for type recognition and time location of combined power quality disturbance," *IEEE Trans. Ind. Informat.*, vol. 15, no. 8, pp. 4481–4493, Aug. 2019.

[37] W. Wang, C. Chen, W. Yao, K. Sun, W. Qiu, and Y. Liu, "Synchrophasor data compression under disturbance conditions via cross-entropy-based singular value decomposition," *IEEE Trans. Ind. Informat.*, vol. 17, no. 4, pp. 2716–2726, Apr. 2021.

[38] P. Costamagna, A. De Giorgi, G. Moser, L. Pellaco, and A. Trucco, "Data-driven fault diagnosis in SOFC-based power plants under off-design operating conditions," *Int. J. Hydrogen Energy*, vol. 44, no. 54, pp. 29002–29006, Nov. 2019.

[39] L. Zhang and D. Zhang, "Domain adaptation extreme learning machines for drift compensation in E-nose systems," *IEEE Trans. Instrum. Meas.*, vol. 64, no. 7, pp. 1790–1801, Jul. 2015.

[40] J. Han, H. Liu, H. Xiong, and J. Yang, "Semi-supervised air quality forecasting via self-supervised hierarchical graph neural network," *IEEE Trans. Knowl. Data Eng.*, vol. 35, no. 5, pp. 5230–5243, May 2023.

[41] Z. Qu, X. Liu, and M. Zheng, "Temporal-spatial quantum graph convolutional neural network based on Schrödinger approach for traffic congestion prediction," *IEEE Trans. Intell. Transp. Syst.*, vol. 24, no. 8, pp. 8677–8686, Aug. 2023.

Hui Zhang received the B.S. degree in Internet of Things engineering from Shandong Jianzhu University, Jinan, China, in 2022. He is currently pursuing the Ph.D. degree in control engineering with the School of Control Science and Engineering, Shandong University, Jinan.

He has authored or co-authored more than ten international journal and conference papers, particularly in IEEE TRANSACTIONS ON INDUSTRIAL INFORMATICS and IEEE TRANSACTIONS ON INSTRUMENTATION AND MEASUREMENT. His current research interests include hydrogen safety, machine learning, and computational intelligence.

Mr. Zhang has served as a reviewer for several international conferences and journals, such as IEEE TRANSACTIONS ON FUZZY SYSTEMS and IEEE TRANSACTIONS ON INDUSTRY APPLICATIONS.

Guangyao Fan received the M.S. degree in energy and power from North China Electric Power University, Baoding, China, in 2023. He is currently pursuing the Ph.D. degree in control theory and control engineering with Shandong University, Jinan, China.

His current research interests include modeling, planning, and optimization of hydrogen energy systems.

Jiaxin Zhang received the M.S. degree in power engineering and engineering thermophysics from Shandong University, Jinan, China, in 2024, where she is currently pursuing the Ph.D. degree with the Institute of Thermal Science and Technology.

Her current research interests include hydrogen risk assessment and analytical models of cryogenic hydrogen jets.

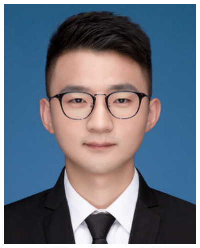

Lizhi Zhang received the B.S. degree in automation from Qingdao University, Qingdao, China, in 2016, and the M.S. degree in control engineering and the Ph.D. degree in control theory and control engineering from Shandong University, Jinan, China, in 2019 and 2024, respectively.

He is currently with Shandong Police College, Jinan. His research interests include integrated energy system planning and optimization.

Xuefang Li received the Ph.D. degree in engineering thermophysics from Tsinghua University, Beijing, China, in 2016.

From 2014 to 2015 and 2018, he worked as a Visiting Researcher with Sandia National Laboratories, Livermore, CA, USA, where he participated in the DOE Hydrogen and Fuel Cells Program. He collaborated on hydrogen safety studies aimed at facilitating the commercialization of hydrogen energy. In 2023, he worked as a Visiting Researcher with Nanyang Technological University, Singapore. He is currently an Associate Professor with the Institute of Thermal Science and Technology, Shandong University, Jinan, China. He has co-authored over 40 peer-reviewed articles. He serves as the principal investigator for several research projects, including two subprograms of national key R&D projects, two projects funded by the National Natural Science Foundation of China, and multiple industry-sponsored projects. His research interests include hydrogen safety, heat transfer, and microfluidics.

Dr. Li is a committee member of several academic and industry societies, including the Chinese Society of Power Engineering (Youth Working Committee), China Society of Automotive Engineering (Automotive Fire Safety Technology Branch), and the International Hydrogen and Fuel Cell Association (Hydrogen Safety and Equipment Branch). He is also a member of many other societies, including China Renewable Energy Society (CRES), the International Association for Hydrogen Energy (IAHE), and China Fire Protection Association.

Bo Sun (Member, IEEE) was born in Shandong, China, in 1982. He received the B.S. and Ph.D. degrees from Shandong University, Jinan, China, in 2004 and 2009, respectively.

In 2010, he joined Shandong University, where he is currently a Professor with the School of Control Science and Engineering. His research interests include the optimal control of engineering and the optimization of integrated energy systems.